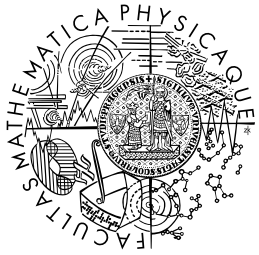

FACULTY
OF MATHEMATICS
AND PHYSICS
Charles University

BACHELOR THESIS

Tomáš Mejsnar

Study of the collision energy at the Belle II experiment

Institute of Particle and Nuclear Physics

Supervisor of the bachelor thesis: Mgr. Radek Žlebčík, Ph.D.
Study programme: Physics

Prague 2024

I declare that I carried out this bachelor thesis on my own, and only with the cited sources, literature and other professional sources. I understand that my work relates to the rights and obligations under the Act No. 121/2000 Sb., the Copyright Act, as amended, in particular the fact that the Charles University has the right to conclude a license agreement on the use of this work as a school work pursuant to Section 60 subsection 1 of the Copyright Act.

In ..... date ....

Author's signature

I would like to thank my supervisor Mgr. Radek Žlebčík, Ph.D., for all of his patience, comments and expertise, without which I would have been lost. I would also like to thank my girlfriend for her patience and for doing all the chores while i was busy working on this thesis for several days straight, especially before the deadline.

Title: Study of the collision energy at the Belle II experiment

Author: Tomáš Mejsnar

Institute: Institute of Particle and Nuclear Physics

Supervisor: Mgr. Radek Žlebčík, Ph.D., Institute of Particle and Nuclear Physics

Abstract: This thesis addresses the measurement of centre-of-mass energy spread $\sigma_{E_{\mathrm{CMS}}}$ in the Belle II experiment. A novel method using the rapidity of muons from $e^+e^- \to \mu^+\mu^-$ interactions was developed. The method involves convolution techniques to deconstruct detector output into detector resolution, physical interaction, and beam energy spread components. Validation through Monte Carlo simulations and application to real data showed $\sigma_{E_{\mathrm{CMS}}}$ of 5.28(1) MeV, closely aligning with other measurements. This approach offers improved precision and reliability over traditional methods, enhancing the accuracy of particle mass measurements. The results support more precise determinations of fundamental parameters, advancing our understanding of the Standard Model.

Keywords: Belle II, calibration, Center-of-mass collision energy

Název práce: Studium energie srážek v experimentu Belle II

Autor: Tomáš Mejsnar

Ústav: Ústav částicové a jaderné fyziky

Vedoucí bakalářské práce: Mgr. Radek Žlebčík, Ph.D., Ústav částicové a jaderné fyziky

Abstrakt: Tato bakalářská práce se zabývá měřením rozptylu rozdělení těžišťové energie $\sigma_{E_{\mathrm{CMS}}}$ v experimentu Belle II. Byla vyvinuta nová metoda využívající rapiditu mionů z interakcí $e^+e^- \to \mu^+\mu^-$. Tato metoda zahrnuje konvoluční techniky k dekompozici výstupu detektoru na komponenty rozlišení detektoru, fyzikální interakce a rozdělení energie svazku. Validace pomocí Monte Carlo simulací a aplikace na reálná data ukázala $\sigma_{E_{\mathrm{CMS}}}$ o hodnotě 5,28(1) MeV, což je v souladu s jinými měřeními. Tento přístup nabízí vyšší přesnost a spolehlivost oproti tradičním metodám, což zlepšuje přesnost měření hmotnosti částic. Výsledky podporují přesnější stanovení základních parametrů a posouvají naše chápání Standardního modelu.

Klíčová slova: Belle II, kalibrace, Těžišťová energie srážek

Contents

Introduction

The Standard Model of particle physics [1] is the theoretical framework that describes the fundamental particles and their interactions. It includes three generations of matter particles: quarks and leptons, which interact via fundamental forces mediated by gauge bosons. The gauge bosons include the photon for electromagnetic interactions, the W and Z bosons for weak interactions, and the gluons for strong interactions. The Higgs boson, discovered in 2012 at the Large Hadron Collider (LHC) [2], is responsible for providing mass to the particles via the Higgs mechanism [1].

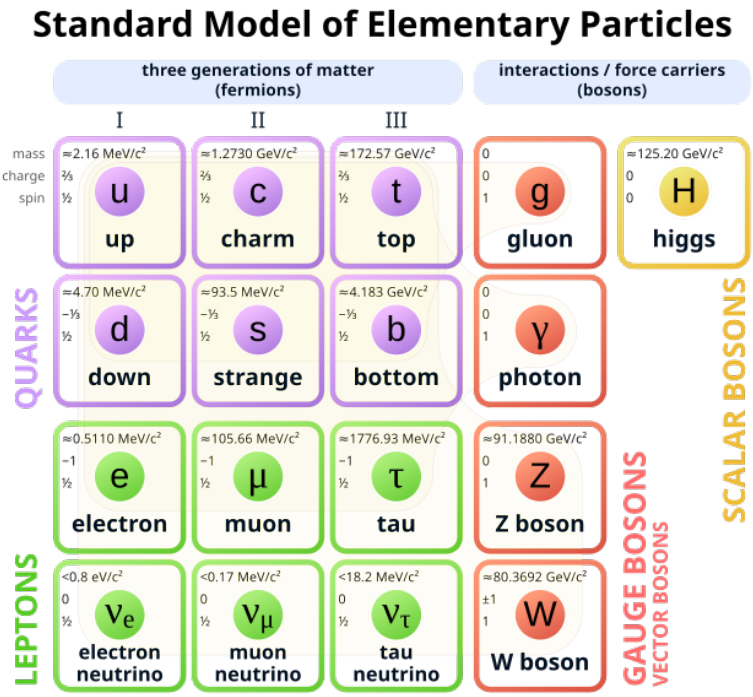

Figure 1 The Standard Model of Elementary Particles [3]

Despite successfully explaining a wide range of phenomena, the Standard Model has limitations. It does not account for gravity, dark matter, or the matter-antimatter asymmetry observed in the universe. To address these gaps, experiments like Belle II [4] at the SuperKEKB collider in Japan aim to probe beyond the Standard Model by studying the properties of heavy flavor particles, especially B mesons, charmed mesons and the tau leptons [1].

The Belle II experiment, conducted at the SuperKEKB collider, studies electron-positron collisions to provide a clean environment for exploring the properties of particles produced in these interactions. One of these possible measurements is the precise determination of the tau lepton mass, a fundamental parameter of the Standard Model. The tau lepton is the heaviest of the leptons and plays a crucial role in testing the validity of the Standard Model. Precise measurement of the tau lepton mass is essential for understanding its properties and interactions.

The accuracy of tau mass measurement is limited by the knowledge of the

momentum scale of the tau lepton decay products and of the collision energy, specifically the centre-of-mass (CM) energy E_{CMS} defined as $E_{\text{CMS}} = \sqrt{(p_{e^+} + p_{e^-})^2}$, where $p_{e^{+/-}}$ are electron/positron 4-momenta. This energy fluctuates slightly between collisions and is described by a probability distribution—a Gaussian curve. The author will develop a new method to measure the parameters of this distribution, especially the spread σ, using $e^+e^- \to \mu^+\mu^-$ interactions recorded by the Belle II detector. To our knowledge, this type of interaction has never been used for energy spread measurement in the Belle II or competing experiments. Better knowledge of the spread σ also allows for a more precise measurement of the central value of the CM collision energy. Improving the calibration of CM energy will enhance the precision of particle mass determinations and other important measurements in the experiment. For example, monitoring if the SuperKEKB truly runs at the $\Upsilon(4S)$ peak energy, which corresponds to the maximal production rate of the B mesons [4, 5].

The Belle experiment, Belle II's predecessor, made significant contributions to the field of particle physics, including the observation of CP violation in B meson decays, which provided crucial tests of the Standard Model and contributed to the awarding of the 2008 Nobel Prize in Physics to Yoichiro Nambu, Makoto Kobayashi and Toshihide Maskawa for their work on CP violation [6]. The SuperKEKB collider, an upgrade of the KEKB collider, achieves higher luminosity by employing a novel design that reduces the beam size at the interaction point, allowing for more frequent collisions focused to a smaller interaction region [4].

The Belle II experiment involves extensive international collaboration. More than 1000 scientists from around the world contribute to the detector's development, operation, and data analysis, ensuring a diverse and comprehensive approach to exploring fundamental questions in particle physics.

1 The Belle II Experiment and the SuperKEKB Collider

The Belle II experiment, conducted at the SuperKEKB collider in Tsukuba, Japan, is a particle physics research project designed to explore the fundamental forces and particles that constitute the universe. The Belle II experiment aims to provide insights into phenomena such as *CP* violation, rare decays, and new physics beyond the Standard Model. The SuperKEKB collider (Figure 1.1), which collides 7 GeV electrons with 4 GeV positrons, is engineered to achieve a peak luminosity of 8×10^{35} cm^{-2}s^{-1} [4], 40 times greater than that of its predecessor, KEKB, facilitating a significantly higher rate of collision events, producing 5×10^{10} tau-pair events per 8 years and enhancing the potential for new discoveries [4]. Like Belle or BaBar experiments, Belle II runs at the $\Upsilon(4S)$ resonance, which decays in 99% to $B\bar{B}$. At the heart of the Belle II experiment is a sophisticated suite of detectors, each designed to measure various aspects of the particles produced in collisions. These detectors collectively form a comprehensive system capable of high-precision tracking, particle identification, energy measurement, and muon detection. The key components of this system are detailed below.

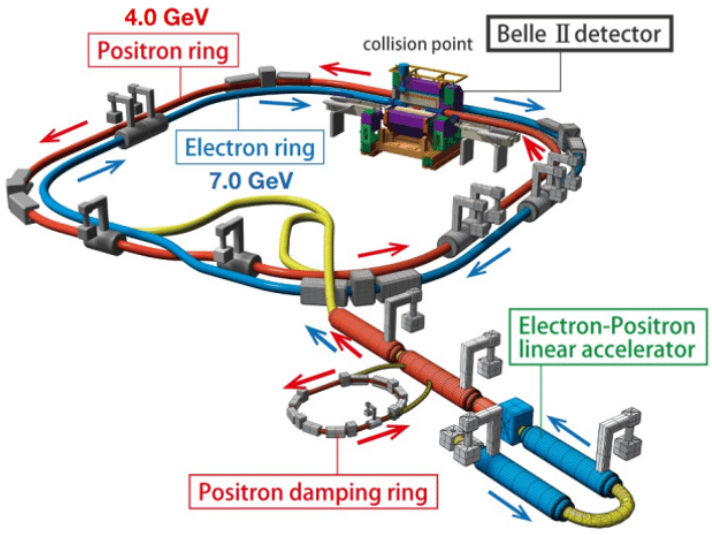

Figure 1.1 The SuperKEKB Collider [7]

1.1 Vertex Detector (VDX)

The Vertex Detector (VDX) (Figure 1.2) is responsible for precisely tracking the paths of particles, especially the short-lived B mesons, as they emerge from the collision point, known as the interaction point. The VDX is composed of two main sub-detectors: the Pixel Detector (PXD) and the Silicon Vertex Detector (SVD) [4, 8].

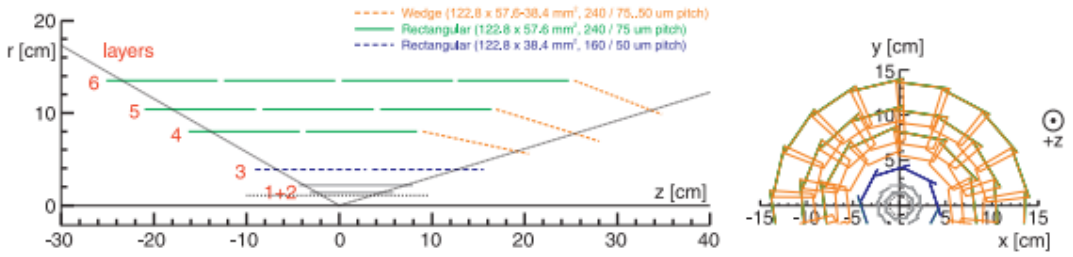

Figure 1.2 A schematic view of Belle II's VDX [4]

1.1.1 Pixel Detector (PXD)

The Pixel Detector (PXD) is the innermost layer of the VDX, located about 1.4-2.2 centimetres from the interaction point. It uses advanced pixel sensors to provide high-resolution tracking of particles. The PXD consists of two cylindrical layers of DEPFET (Depleted P-channel Field Effect Transistor) pixel sensors. Each sensor has a pixel size of $(50) \times (50 - 85)$ micrometres, allowing for precise measurement of the secondary vertices for example of the B mesons. The small material budget of PXD reduces multiple scattering effects and particle energy loss, ensuring accurate trajectory measurement [4, 8].

1.1.2 Silicon Vertex Detector (SVD)

Surrounding the PXD is the Silicon Vertex Detector (SVD), located about 3.9-13.5 cm from the interaction point, which covers a larger volume and provides additional tracking information. The SVD consists of four layers of double-sided silicon strip sensors arranged in a barrel configuration around the interaction point. Each strip sensor has a pitch of 50 micrometres, allowing for high-resolution measurements of particle tracks. The combination of the PXD and SVD enables Belle II to achieve a vertex resolution of approximately 10 micrometers, significantly improving the accuracy of measurements involving the decay vertices of B mesons, e.g. the time-dependent CP violation [4, 8].

1.2 Central Drift Chamber (CDC)

The Central Drift Chamber (CDC) (Figure 1.3) is the primary tracking device for charged particles in Belle II. It is a large cylindrical chamber filled with a gas mixture of helium and isobutane. The CDC is 2.3 meters long and has a radius of 1.6 meters. It contains 56 layers of sense and field wires arranged in a helical pattern. As charged particles pass through the CDC, they ionize the gas, creating electron-ion pairs. The electrons drift towards the sense wires, where their arrival times are measured. By analyzing these times, the CDC reconstructs the particles' trajectories. The curvature of the tracks in the CDC, caused by the 1.5 Tesla magnetic field, allows for precise determination of the charged particles' momenta. The CDC also helps identify particles by measuring the ionization energy loss (dE/dx) along their paths, which varies for different particle types [8].

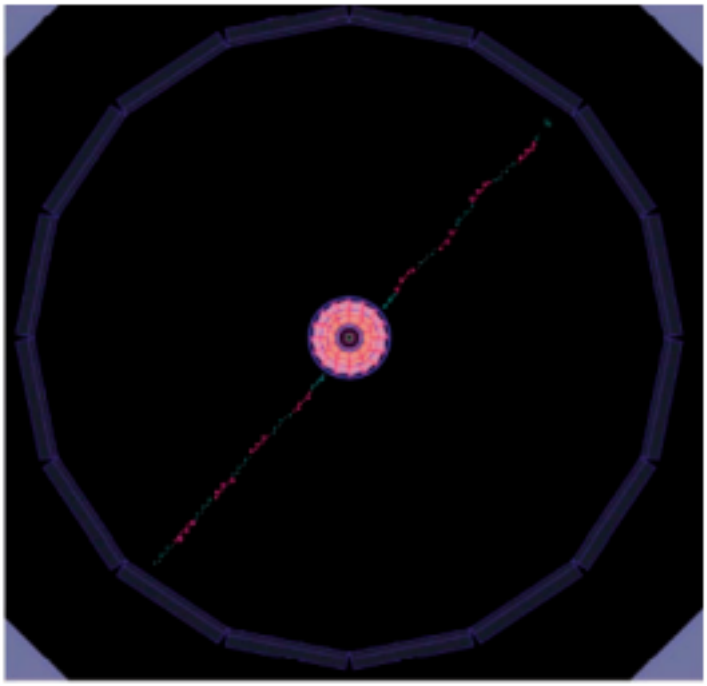

Figure 1.3 A cosmic muon as recoded by the Belle II's CDC [4]

1.3 Particle Identification System (PID)

The Particle Identification System (PID) in Belle II is designed to improve the accuracy of identifying various types of charged particles, such as pions, kaons, and protons. It consists of several sub-detectors that measure the particles' different properties to identify them accurately. The PID likelihoods are obtained from a combination of all inputs, not only TOF and ARICH, but also CDC, ECL, KLM and VXD. For example, muons used in this thesis are characterized by small energy deposits in the calorimeter (ECL), tracks in CDC, and a signal in KLM.

1.3.1 Time-of-Flight (TOF) Counters

The TOF system consists of an array of scintillation counters (Figure 1.4-Left) placed around the CDC. By measuring the time it takes for particles to travel from the interaction point to the TOF counters, the system determines their velocities. Combining this information with the momentum measured by the CDC, the PID system can calculate the particles' masses and identify them [8].

1.3.2 Aerogel Ring Imaging Cherenkov (ARICH) Detector

The ARICH detector (Figure 1.4-Right) uses aerogel, a lightweight material with a refractive index just above that of air, to produce Cherenkov radiation when charged particles pass through it. The angle of the Cherenkov light cone depends on the particle's velocity, which helps distinguish between different types of particles [8].

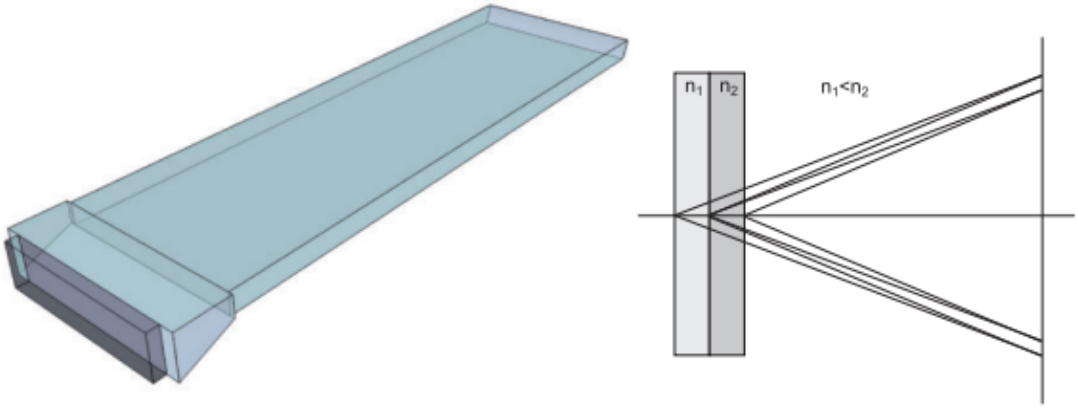

Figure 1.4 Belle II's PID: TOP module counter (Left), ARICH principle of operation (Right) [4]

1.4 Electromagnetic Calorimeter (ECL)

The Electromagnetic Calorimeter (ECL) is designed to measure the energy of electrons and photons produced in collisions. It comprises an array of 8736 thallium-doped cesium iodide (CsI(Tl)) scintillation crystals arranged in a barrel and two endcaps. Each crystal is approximately 30 cm long and 5 cm in cross-section. When high-energy particles strike the crystals, they produce scintillation light proportional to the particles' energy. Photodiodes coupled to the crystals detect this light, and the ECL electronics convert the signals into energy measurements. The ECL has an energy resolution of about 1.6% for electrons and photons with energies around 1 GeV. This high resolution is crucial for studying processes involving electromagnetic interactions, such as the decay of B mesons into final states containing electrons or photons [8].

1.5 K_L^0 and Muon Detector (KLM)

The K_L^0 and Muon Detector (KLM) is designed to detect long-lived neutral kaons (K_L^0) and muons. It consists of alternating layers of resistive plate chambers and iron absorbers positioned outside the ECL. The iron layers absorb most particles except for muons and K_L^0, which can penetrate deeper into the detector. The KLM provides crucial information for identifying muons and reconstructing the trajectories of K_L^0 particles, aiding in studying rare decay processes and CP violation.

The KLM is divided into a barrel section and two endcaps, covering the entire solid angle around the interaction point. It comprises 15 layers of resistive plate chambers (RPCs) interleaved with iron absorber plates. The iron plates stop non-muon particles, while muons, being highly penetrating, pass through and are detected by the RPCs. The RPCs consist of two parallel resistive plates with a gas gap in between. When a charged particle passes through, it ionizes the gas, producing a signal that is read out by the detector electronics. The KLM can also detect K_L^0 particles through their interactions with the iron plates, which produce secondary particles that are detected by the RPCs. The KLM provides excellent muon identification with an efficiency of over 90% and a misidentification rate of

less than 1% [4, 8].

2 Tau lepton mass and E_{CMS}

The tau lepton is a third-generation lepton with a mass significantly higher than that of the electron and the muon, making its precise mass measurement critical for testing the Standard Model's predictions and exploring potential New Physics. Accurate determination of the tau lepton mass can provide insights into the nature of lepton universality and the parameters of electroweak interactions [1], demonstrated in Figure 2.1.

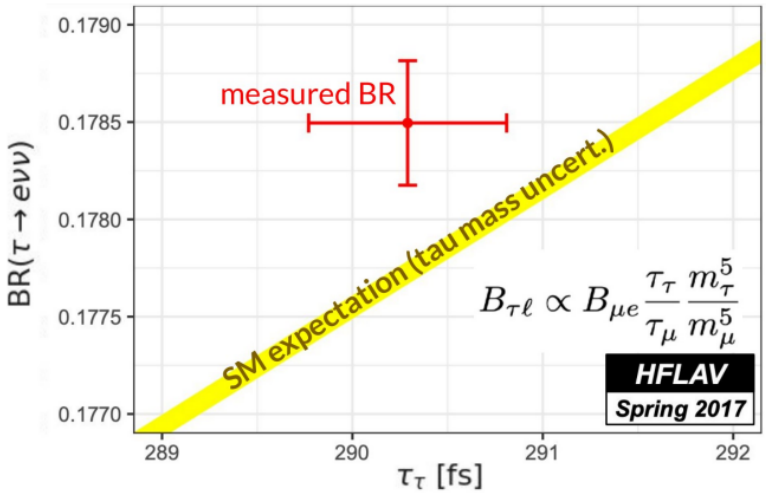

Figure 2.1 The graph illustrates the relationship between tau lifetime and the Branching Ratio (BR) of decaying through the $\tau \to e\nu\nu$ channel (its most common decay channel). The yellow band is the theoretical standard model expectation, with tau mass uncertainty responsible for its width. The red point corresponds to the current experimental value with error bars related to the world-averaged lifetime and the BR [9].

Recent advancements in experimental techniques have led to the most precise measurement of the tau lepton mass to date, achieved by the Belle II experiment [10]. For the Belle II tau mass measurement, researchers led by DESY scientists used data collected from 2019 to 2021 to study the decays of tau leptons into three pions and a tau neutrino from electron-positron collisions at center-of-mass energy about 10.58 GeV, applying a technique initially developed by the ARGUS collaboration at DESY in 1992. This method relies on precise knowledge of the absolute momentum scale of the tau decay products and the collision energy of the electron-positron pairs. The measured tau mass (1777.09 ± 0.14) MeV is consistent with previous results but provides the highest single-measurement precision to date (Figure 2.2), improving our understanding of the tau lepton's properties and the Standard Model [4, 11].
The previous most precise tau mass measurement was accomplished at BES III tau-factory in China [12] using the energy scan technique, where the CM collision energy is varied around the $\tau^+\tau^-$ production threshold, i.e. around $2m_\tau \sim 3.5$ GeV.

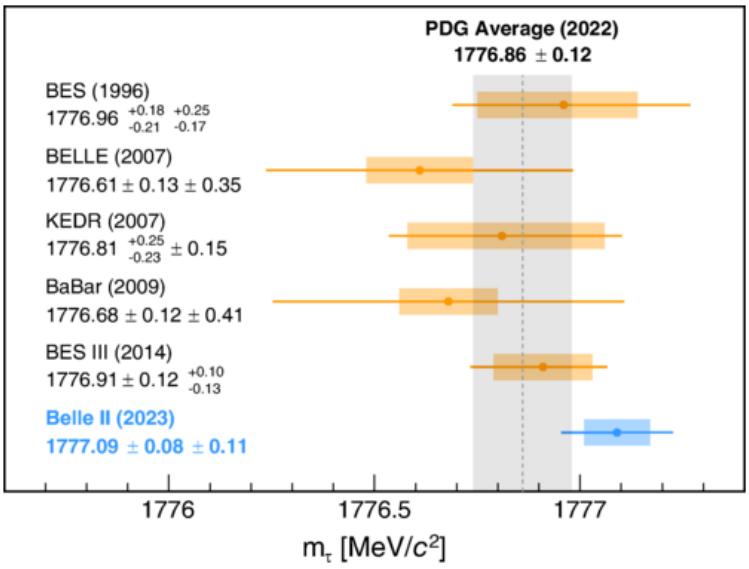

Figure 2.2 The comparison of measured τ mass by leading experiments with statistical and systematic uncertainties [10]

2.1 Impact of the E_{CMS} precision on the τ mass measurement

At B-factories such as Belle II, the measurement of the center-of-mass energy E_{CMS} is pivotal for several reasons. The energy of the collisions directly influences the kinematics and dynamics of the particles produced, including the tau leptons. At Belle II the pseudomass technique [5] is used to measure the tau lepton mass in $\tau \to 3\pi\nu$ decays. The distribution of pseudomass variable, M_{min}, calculated from the τ meson decay products momenta and center-of-mass collision energy E_{CMS} as:

$$M_{\text{min}} = \sqrt{M_{3\pi}^2 + 2\,(E_{\text{CMS}}/2 - E_{3\pi})\,(E_{3\pi} - P_{3\pi})}, \tag{2.1}$$

has a steep drop for $M_{\text{min}} = m_\tau$ which makes this variable sensitive to the value of the tau mass. The initial-state photon radiation and detector resolution lead to the smoothing of the step in the pseudomass M_{min}. The pseudomass, as measured by the Belle II experiment, is shown in Figure 2.3.

The formula for pseudomass M_{min} directly depends on the CMS collision energy E_{CMS}. Employing standard uncertainty propagation technique, it can be shown that:

$$\delta M_{min} = 0.085\,\delta E_{\text{CMS}}. \tag{2.2}$$

This relation indicates that, for example, a 1 MeV shift in the CM energy results in a 0.085 MeV shift in the tau mass.

At Belle II the CMS collision energy was measured with a precision of $\approx$0.8 MeV, which corresponds to 0.07 MeV uncertainty on the tau mass, which makes it the dominant systematic uncertainty source (see Table 2.1).

It is known that the collision energy at SuperKEKB has varied during the data-taking period, therefore a precise measurement of the tau mass relies on an accurate determination of the beam energy as the function of time [5].

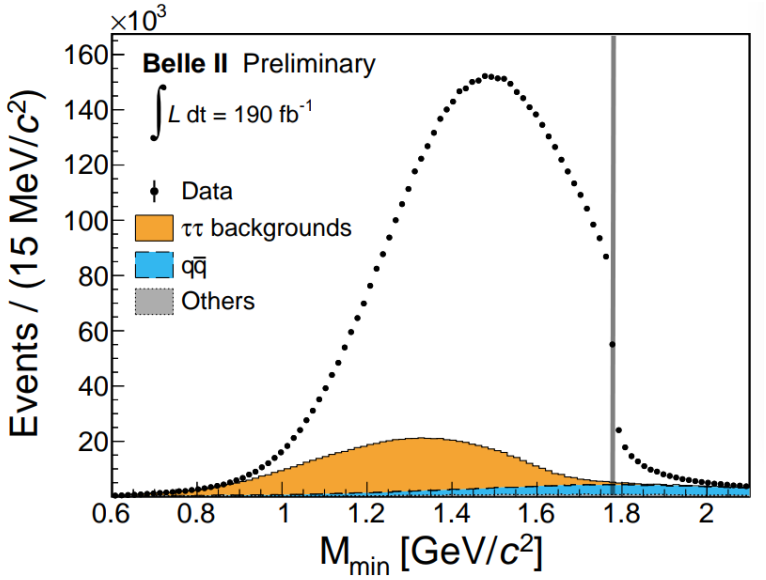

Figure 2.3 Spectrum of M_{min} in experimental data (dots) as measured at Belle II [10], along with simulated background contributions from $e^+e^- \to \tau^+\tau^-$ events with decays other than $\tau^- \to \pi^-\pi^+\pi^-\nu_\tau$ (orange area with solid line), $e^+e^- \to q\bar{q}$ events (blue area with dashed line), and other background sources (gray area with dotted line). The value of the tau mass is indicated by a vertical gray line.

Source	**Uncertainty** [MeV/c^2]
Knowledge of the colliding beams:	
Beam-energy correction	0.07
Boost vector	< 0.01
Reconstruction of charged particles:	
Charged-particle momentum correction	0.06
Detector misalignment	0.03
Fit model:	
Estimator bias	0.03
Choice of the fit function	0.02
Mass dependence of the bias	< 0.01
Imperfections of the simulation:	
Detector material density	0.03
Modeling of ISR, FSR and τ decay	0.02
Neutral particle reconstruction efficiency	≤ 0.01
Momentum resolution	≤ 0.01
Tracking efficiency correction	≤ 0.01
Trigger efficiency	< 0.01
Background processes	< 0.01
Total	0.11

Table 2.1 Summary of systematic uncertainties in the Belle II τ-mass measurement [10]. The dominant sources are related to E_{CMS} "Beam-energy correction" and to the momentum scale of charged pions into which tau decays ("Charged-particle momentum correction").

2.2 Measurement of E_{CMS} using B meson energy in the CMS

The main method used for measuring the center-of-mass energy (E_{CMS}) in electron-positron collisions is through the process $e^+e^- \to B\bar{B}$. In this process, electron and positron beams collide to produce pairs of bottom quarks, which subsequently hadronize into B mesons. The kinematics of these B mesons in CMS can be precisely measured, allowing for an accurate determination of E_{CMS}. Charged or neutral B mesons are used because their mass is only slightly below the $E_{\mathrm{CMS}}/2$. Consequently, the produced B mesons are slow, and the non-relativistic formula can be used to calculate the B mesons energy in the CMS:

$$E_B^* = m_B + \frac{p_B^{*2}}{2m_B}, \tag{2.3}$$

where E_B^*, m_B, and p_B^* are one B meson's energy, mass, and momentum in CMS. The mass term is known with very high precision, especially thanks to the LHCb [13, 14], the second term is much smaller, but also with much higher uncertainty. Consequently, the systematic uncertainties originating from the precision of the m_B and from the second term are comparable. An example of the E_B^* measurement can be seen in Figure. 2.4, where the width of the observed peak is mostly driven by the beam energy spread.

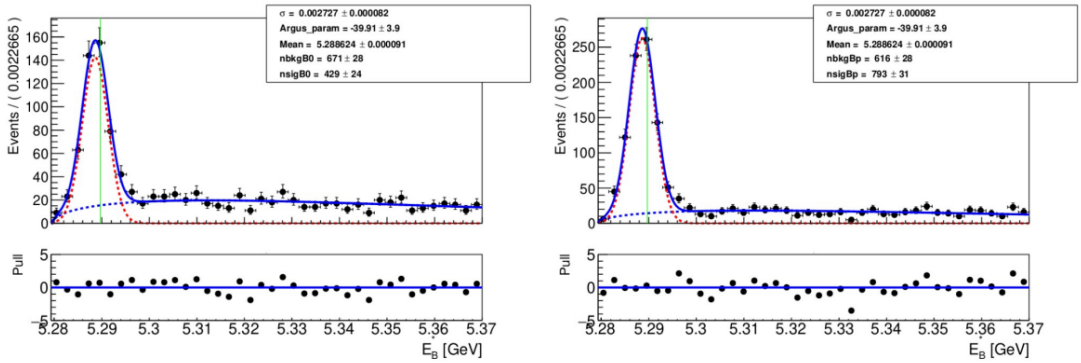

Figure 2.4 Measured B meson energy in CMS corresponding to $E_{\mathrm{CMS}}/2$ for B^0 (Left) and B^+ (Right) [5]. Blue lines represent the fits to the observed data. The precise E_{CMS} is obtained from the "Mean" and "σ" parameters of the Gaussian peak by applying energy corrections to correct for $\Upsilon(4S)$ shape and photon radiation. Nominal collision energy corresponding to the $\Upsilon(4S)$ mass is depicted as a vertical green line.

It is important to note that E_B^* do not directly correspond to the $E_{\mathrm{CMS}}/2$, partially it is because of the process $e^+e^- \to B\bar{B}\gamma$, i.e. when part of the energy is radiated via photon and B meson energy do not correspond to $E_{\mathrm{CMS}}/2$ anymore. The second reason is the energy dependence of the $e^+e^- \to B\bar{B}$ cross-section, in other words, the shape of the $\Upsilon(4S)$ resonance. This effect is related to the E_{CMS} spread, the main topic of this thesis. The E_{CMS} slightly fluctuates between the collisions and its spectrum can be described by the Gaussian distribution. When the mean E_{CMS} is slightly below the $\Upsilon(4S)$ resonance mass, which was the case for most of the Belle II data, as the collision energy fluctuates event-by-event, sometimes the E_{CMS} value is closer to the resonance peak, other times

it is further away. For events where the E_{CMS} is closer to the resonance mass, the $B\bar{B}$ production cross section is higher, i.e. it is more likely to produce $B\bar{B}$. Consequently, the distribution of $2E_B^*$ does not have the same mean value as the E_{CMS} but is pushed towards the $\Upsilon(4S)$ mass. The higher the E_{CMS} spread, the higher the impact. When B mesons are used for the E_{CMS} determination, the measured $2E_B^*$ value has to be corrected for effects of the photon emissions and the energy dependence of the $B\bar{B}$ cross section using so-called energy corrections. The main uncertainty of these corrections stems from the uncertainty in the $\Upsilon(4S)$ energy shape and from the value of the E_{CMS} energy spread.

Sources of systematic uncertainties of the $e^+e^- \to B\overline{B}$ method of E_{CMS} are shown in Table 2.2 and described below [5, 11, 10], for each systematic source, the symmetrized uncertainty is provided.

- Detector uncertainty $\Delta 2E_B^*$, which is related to the uncertainty of measuring momenta of B meson decay products (0.05 MeV).
- Uncertainty of E_{CMS} spread σ_{E^*} bias, which is exactly what our method is trying to lower (0.22 MeV).
- Uncertainty caused by limited knowledge of the shape of the $\Upsilon(4S)$ resonance E(BaBar), from which the B mesons originate. Measured by Belle and BaBar experiment, which can also be lowered using our method by measuring the $\Upsilon(4S)$ resonance shape at Belle II (0.50 MeV).
- B meson mass precision $M_B^{\text{PDG ave.}}$, which is taken from the world mean, dominated by LHCb measurement[1] (0.48 MeV).

	$\langle\sqrt{s}\rangle$	$\langle\sqrt{s} - \sqrt{s_{\text{central}}}\rangle$
	[GeV]	[MeV]
$2E_B^*$	10.57618	-0.47
$\Delta 2E_B^*$	[10.57659, 10.57670]	[-0.06, 0.04]
σ_{2E^*} bias	[10.57643, 10.57687]	[-0.22, 0.22]
$\sqrt{s}$	10.57665	-
E (BaBar)	[10.57610, 10.57709]	[-0.55, 0.44]
$M_B^{\text{PDG ave.}}$	[10.57617, 10.57713]	[-0.48, 0.48]
total	[10.57587, 10.57735]	[-0.78, 0.70]

Table 2.2 Summary of the average $2E_B^*$ and $\langle\sqrt{s}\rangle$ values used in the m_τ measurement and the corresponding uncertainties [5]. E_{CMS} is sometimes labeled as $\langle\sqrt{s}\rangle$, where s is one of the three Mandelstam variables describing $2 \to 2$ interactions [16].

2.3 Measurement of E_{CMS} using the invariant mass of muons in $e^+e^- \to \mu^+\mu^-$ interactions

An alternative and complementary method for measuring E_{CMS} is through the process $e^+e^- \to \mu^+\mu^-$, where electron-positron collisions result in the production of

[1] There is a new B^+ mass measurement from LHCb [15], which was not available at time of the Belle II tau mass measurement and can reduce this systematic uncertainty.

muon pairs. This method is particularly advantageous due to the clean signatures of muons in particle detectors and the well-understood nature of their interactions. This approach also benefits from high statistical precision and is insensitive to the shape of the $\Upsilon(4S)$ resonance. However, it suffers from large systematic uncertainties in the absolute scale of the invariant $\mu\mu$ mass (Figure 2.5) related to the systematic uncertainty of the muons momentum scale, in particular, due to imprecise knowledge of the detector's magnetic field. The width of $M(\mu\mu)$ is

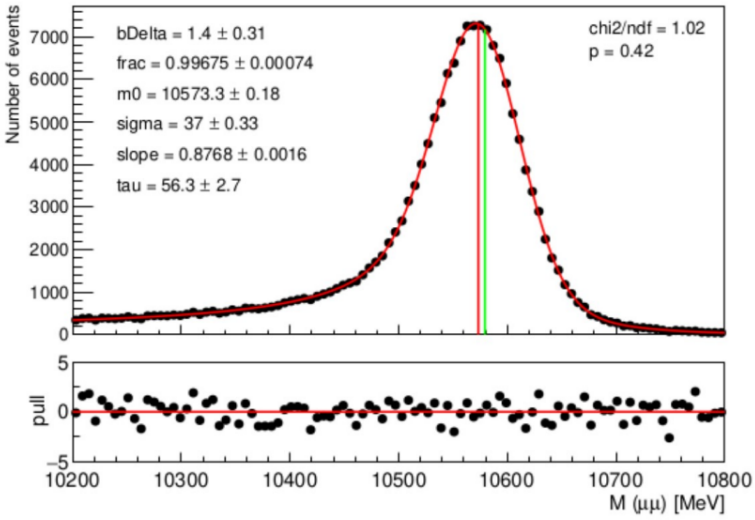

Figure 2.5 The invariant $\mu\mu$ mass. The collision energy is related to the position of the peak, i.e. parameter "m0" of the fitted curve (depicted as the red vertical line in the plot). The nominal beam energy corresponding to the $\Upsilon(4S)$ mass is depicted as a green vertical line.

driven by the detector resolution and is about 40 MeV. In comparison, the energy spread of about 5 MeV is insignificant, making it impossible to measure the energy spread from the $M(\mu\mu)$ variable.

To conclude, the method based on the $\mu\mu$ invariant mass is good for tracking changes in E_{CMS} in time but cannot be a baseline for the absolute E_{CMS} measurement due to the high momentum scale uncertainty of the muons.

2.4 Measurement of E_{CMS} spread using the rapidity of muons in $e^+e^- \to \mu^+\mu^-$ interactions

The third method, which is novel and described in this work, measures the E_{CMS} spread using the rapidity of muons in $e^+e^- \to \mu^+\mu^-$ interactions. This method has the following advantages:

- High statistical precision.
- Independence from the shape of the $\Upsilon(4S)$ resonance.
- Applicability to data taken at energies outside the $\Upsilon(4S)$ resonance.

However, this method only measures the spread of E_{CMS} (i.e., the sigma of the Gaussian distribution) rather than the mean value.

For the most precise determination of E_{CMS}, a combination of all three methods should be employed. Each method contributes its strengths:

- The B meson energy method provides both the mean and spread of E_{CMS}, but has low statistical precision and suffers from theoretical uncertainty related to the $\Upsilon(4S)$ shape.
- The invariant mass of muons method offers high statistical precision to monitor the E_{CMS} time variations and is not biased by the $\Upsilon(4S)$ resonance.
- The rapidity of the muons method supplies an accurate measure of the E_{CMS} spread.

By integrating the complementary advantages of each method, it will be possible to achieve a more accurate and reliable measurement of E_{CMS}. This combined approach would mitigate the individual weaknesses and leverage the statistical and systematic strengths, ultimately leading to a robust determination of E_{CMS} crucial for precise tau mass measurement and other analyses at Belle II and other experiments.

3 The E_{CMS} spread measurement from di-muons

Using simulated data of $e^+e^- \to \mu^+\mu^-$ events, we aim to deconstruct the detector output into convolution of functions representing detector resolution R_{det}, physics behind the interaction R_{truth} and the spread in ee rapidity, which corresponds directly to E_{CMS} spread. The application of this deconvolution on real detector output should then yield an accurate E_{CMS} spread.

3.1 Implementation and Tools

In this project, we utilize `C++` in conjunction with the `ROOT` software library [17].

3.1.1 C++

`C++` is a versatile and widely-used programming language known for its performance and efficiency. Developed as an extension of the `C` language, `C++` supports object-oriented programming. The Belle II analysis software (`basf2`) as well as `ROOT` analysis framework are written mostly in the `C++` language.

3.1.2 ROOT Software Library

`ROOT` is an open-source software framework developed by CERN, specifically designed for data analysis in high-energy physics. It provides a comprehensive set of tools for data handling, statistical analysis, visualization, and storage. The library is written in `C++` and offers a seamless interface with this language, enabling efficient manipulation of large datasets.

Key features of `ROOT` that we will be using include:

- **Data Storage and Access**: `ROOT`'s file format (`ROOT` files) allows for efficient storage and retrieval of large volumes of data. The `TTree` and `TBranch` classes facilitate hierarchical data organization, enabling structured data analysis.
- **Statistical Analysis**: `ROOT` includes a wide range of statistical functions and methods for data fitting, especially the `TF1` function class. Its fitting algorithm, based on `MINUIT` minimization package [18], is widely used for parameter estimation and uncertainty quantification.
- **Visualization**: `ROOT` provides many visualization tools for creating graphical representations of data. The `TCanvas`, `TH1`, and `TGraph` classes allow for the creation of histograms, scatter plots, and other graphical displays. We will also use Plotting helper [19], a small package containing utilities to make plotting in `ROOT` more user-friendly.

3.2 Monte Carlo Simulation

Monte Carlo methods [20] are widely used in particle physics to simulate complex processes and predict experimental measurement outcomes. In this project, we employ the KKMC generator [21] to model electron-positron to muon-antimuon (including photon emissions) events and GEANT4 [22] to account for detector effects. GEANT4 contains a whole 3D model of the detector with all the relevant materials. It models the passage of particles through the detector's material, deposited energy, and digitalization of the results.

The simulation generates three types of particle four-momenta:

1. The four-momenta of the incoming electrons and positrons, denoted as p_{e^+} and p_{e^-}.

2. The four-momenta of the outgoing truth-level muons, denoted as $p_{\mu^+}^{\text{truth}}$ and $p_{\mu^-}^{\text{truth}}$.

3. The four-momenta of the outgoing detector-level muons, as reconstructed by the detector (the effective detector output), denoted as $p_{\mu^+}^{\text{det}}$ and $p_{\mu^-}^{\text{det}}$.

Monte Carlo simulations provide a detailed description of the kinematics involved in the particle interactions. By generating a large number of simulated events, we can statistically analyze the properties and behavior of the particles. The simulations take into account both the theoretical model of the interaction and the response of the detector, allowing for a realistic representation of the experimental setup.

The four-momenta of the incoming electrons and positrons (p_{e^+} and p_{e^-}) serve as the initial conditions for the simulation. Those four-momenta are not fixed, they slightly vary for each event, and these variations are assumed to obey the Gaussian probability distribution. The nominal energies of the particles in the electron and positron beams are 7.007 GeV and 4.000 GeV and beams collide with the nominal crossing angle of 83 mrad (i.e. not exactly head-on). Nominal energy spreads are 4.41 MeV for electrons and 3.08 MeV for positrons [8, 23]. These parameters lead to a nominal CM collision energy of 10.579 GeV with a spread of 5.26 MeV which is also Gaussian. The real values of the CM energy and the spread differ from its nominal values, and the goal of the thesis is to measure the real value of the CM spread using $e^+e^- \to \mu^+\mu^-$ interactions.

The generated four-momenta of the outgoing muons ($p_{\mu^+}^{\text{truth}}$ and $p_{\mu^-}^{\text{truth}}$) reflect the theoretical predictions of the interaction. To incorporate the effects of the detector resolution, these momenta are further processed to obtain the effective detector output ($p_{\mu^+}^{\text{det}}$ and $p_{\mu^-}^{\text{det}}$).

3.3 Data Transformation

First, we arranged the four-momenta into the `TLorentzVector` form for easier manipulation. Next, we moved from the laboratory frame (LAB) to the center of mass system (CMS). The center of mass system is a reference frame in which the total momentum of the system is zero, making it particularly useful for studying particle collisions as it simplifies the analysis of kinematic properties.

Our transformation also rotates the system in a way that ensures the collisions of particles happen along the z-axis.

To achieve this transformation, we developed a custom function that performs Lorentz transformations. The Lorentz transformation is a linear transformation that preserves the spacetime interval between events in special relativity, accounting for both time dilation and length contraction. This transformation is essential for accurately converting the four-momenta between different reference frames. At Belle II the particles do not collide exactly head-on, consequently, 5 parameters are needed to describe the Lorentz transformation to the CMS. The three of them are components of the velocity vector of the CMS and the remaining two are the rotation angles that ensure that in CMS the particles collide along z-axis. For the analysis of MC events, the parameters of the Lorentz transformations are derived from the truth average momenta of the incoming particles, whereas for data the parameters of the transformation are obtained from dedicated calibrations measuring the CMS velocity vector (so-called boost vector) and the incoming electron direction in the boosted frame [24].

It is important to notice that by our definition, the parameters of the Lorentz transformation do not incorporate residual event-by-event variations of the electron(positron) energies caused by the energy spread of the beams, i.e. the transformation is derived from the central values of the beam's momenta. Consequently, on average, the total momentum in the CM system is zero, but there are small fluctuations on the event-by-even basis due to the beam energy spreads - something we intend to measure. This mimics the situation with the real data, where we also know only values averaged over many events.

Once in the CMS, we converted the four-momenta of all muons into rapidity along the z-axis. Rapidity is a measure used in particle physics that is related to the angle w.r.t. z-axis and the particle velocity. It is particularly useful because, unlike regular velocity, rapidity is additive under Lorentz transformations along the z-axis. The rapidity y is defined in terms of the particle's energy E and the longitudinal component of its momentum p_z as follows:

$$y = \frac{1}{2} \ln \left(\frac{E + p_z}{E - p_z} \right) \tag{3.1}$$

For highly relativistic particles with velocities close to the speed of light, rapidity becomes almost identical to pseudorapidity, which depends only on the polar angle θ of the particle's momentum relative to the beam axis and is given by:

$$\eta = - \ln \left(\tan \frac{\theta}{2} \right) \tag{3.2}$$

This approximation is significant because our rapidity y depends primarily on the angle θ and only slightly on the magnitude of the momentum p. Since the precision of measuring the angle (direction of the particle's flight) is much higher than that of measuring the magnitude of the momentum, which is related to the curvature of the track, this relationship allows for more accurate measurements.

For each event, the muons' rapidity y is calculated as the average of the rapidities of the two muons with opposite charges, i.e., μ^+ and μ^-. At the

detector-level the muons rapidity is:

$$y_{\text{det}} = \frac{y^{\mu^+}_{\text{det}} + y^{\mu^-}_{\text{det}}}{2} \tag{3.3}$$

Similarly, the truth-level muons rapidity y_{truth} is calculated as:

$$y_{\text{truth}} = \frac{y^{\mu^+}_{\text{truth}} + y^{\mu^-}_{\text{truth}}}{2} \tag{3.4}$$

For the electrons and positrons, the summed rapidity of both beams y_{ee} (further just 'beam rapidity') is calculated using the boost vector β. A boost vector describes the velocity of one reference frame relative to another and is essential for calculating the rapidity of particles in different frames. The rapidity y_{ee} of the e^+e^- system is given by:

$$y_{\text{ee}} = \text{atanh}\frac{p_{\text{ee}}}{E_{\text{ee}}}, \tag{3.5}$$

where p_{ee} is the size of the total three-momentum of the electron-positron system and E_{ee} is the total energy.

Then, we created histograms containing all the events to visualize the distributions of the different rapidities. The histograms include:

- **The e^+e^- rapidity histogram** (y_{ee} as defined in (3.5))
- **Truth-level muons rapidity histogram** (y_{truth} as defined in (3.4))
- **Detector-level muons rapidity histogram** (y_{det} as defined in (3.3))

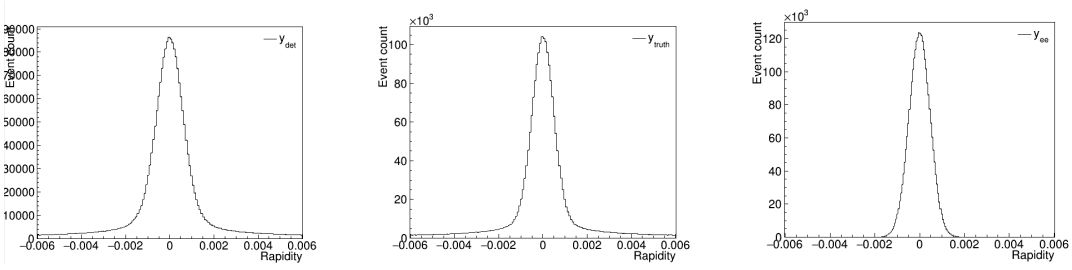

(a) Detector-level muons rapidity histogram (b) Truth-level muons rapidity histogram (c) The ee rapidity histogram

Figure 3.1 The ee, Truth-level and Detector-level rapidity histograms

At first glance, all the histograms (Figure 3.1) seem to follow Gaussian distribution, but that is the case only for 3.1(c). The other two have slowly decreasing tails, like a power function which is mostly caused by the photons radiation.
Additionally, we created resolution histograms to analyze the differences between the calculated rapidities:

- **Total resolution histogram** ($y_{\text{det}} - y_{\text{ee}}$ for each event)
- **Truth resolution histogram** ($y_{\text{truth}} - y_{\text{ee}}$ for each event)

- **Detector resolution histogram** ($y_{\text{det}} - y_{\text{truth}}$ for each event)

To further verify the accuracy of our transformations and the behavior of our simulation, we generated two-dimensional histograms and sliced both of them into five sectors to ensure that the resolutions don't depend on the input:

- **Two-dimensional histogram slices of Beam rapidity vs. Truth resolution** (y_{ee} vs. $y_{\text{truth}} - y_{\text{ee}}$)
- **Two-dimensional histogram slices of Truth-level muon rapidity vs. Detector resolution** (y_{truth} vs. $y_{\text{det}} - y_{\text{truth}}$)

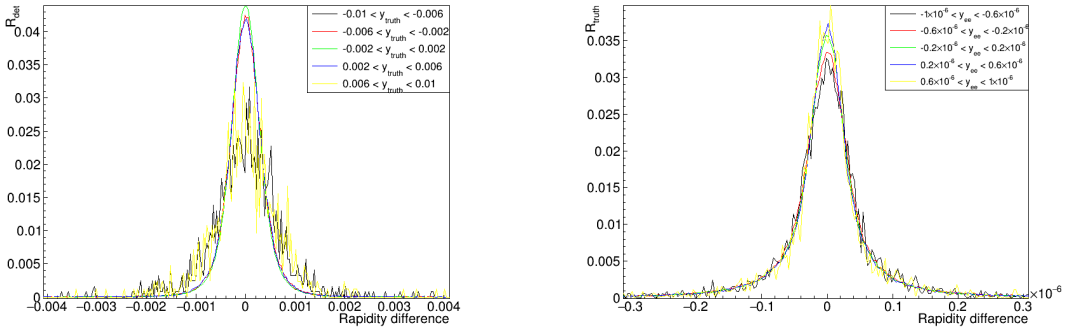

(a) Truth-level muons rapidity vs. Detector resolution

(b) The ee rapidity vs. Truth resolution

Figure 3.2 Slices of two-dimensional histograms showing the relationship between the resolution functions and their input.

These graphs (Figure 3.2) demonstrate that the resolution functions do not heavily depend, at least in the relevant intervals, on their input, which makes them reliable to use and are not tailored just to the data they were created on.

3.4 Convolution

Convolution is a mathematical operation that combines two functions to produce a third function, representing how the shape of one function is modified by the other. It is commonly used in signal processing, physics, and statistics to analyze the effects of various filters and system responses. The convolution of two functions f and g is defined as:

$$(f \otimes g)(x) = \int_{-\infty}^{\infty} f(t)g(x-t)\,dt \tag{3.6}$$

Our motivation is to deconstruct the Detector-level muon rapidity ($f_{\mu\mu}(y_{\text{det}})$) into three components: Detector Resolution Function (R_{det}), Truth Resolution Function (R_{truth}) and Beam Rapidity Spread ($f_{ee}(y_{\text{ee}})$):

$$f_{\mu\mu}(y_{\text{det}}) = R_{\text{det}} \otimes R_{\text{truth}} \otimes f_{ee}(y_{\text{ee}}) \tag{3.7}$$

3.4.1 Analytical Convolution of Two Functions

In a few cases, the convolution of two functions can be computed analytically. For instance, when convoluting a Gaussian function with another Gaussian function, the resulting function is yet another Gaussian function with mixed parameters. The degree of smearing depends on the σ parameter of the Gaussian function. Analytical convolutions like these can be computed using software such as Wolfram Alpha [25].

3.4.2 Numerical Convolution of Two Functions

When an analytical solution is not feasible, the convolution can be computed by numerical integration. We will be using the Gauss-Kronrod quadrature method [26], which is precise and uses only a handful of points, so it's fast. This way, we will convolute a symmetrical double-sided Crystal Ball function [27] with a Gaussian function. The Crystal Ball function is commonly used in high-energy physics to model the resolution of particle detectors, combining a Gaussian core with a power-law tail to account for non-Gaussian resolution effects. The symmetrical double-sided Crystal Ball function (from now denoted just as CB) has power tails on both sides, and because it is symmetrical, they are the same. The functional form of the CB function is:

$$\mathrm{CB}(x;\alpha,n,\bar{x},\sigma) = N \begin{cases} \exp\left(-\frac{(x-\bar{x})^2}{2\sigma^2}\right) & \text{for } -\alpha < \frac{x-\bar{x}}{\sigma} < \alpha \\ A\left(B - \frac{x-\bar{x}}{\sigma}\right)^{-n} & \text{for } \frac{x-\bar{x}}{\sigma} \leq -\alpha \\ A\left(\frac{x-\bar{x}}{\sigma} - B\right)^{-n} & \text{for } \alpha \leq \frac{x-\bar{x}}{\sigma} \end{cases} \tag{3.8}$$

where A and B are constants defined to ensure continuity and N ensures that the function is normalized to 1.

Another way of computing the convolution of two functions is by using the Fourier Transform (FT) [28], specifically the Fast Fourier Transform (FFT). The Fourier transform is a mathematical transformation that decomposes a function into its constituent frequencies. The FFT is exactly the same transformation, just using a different - faster algorithm that reduces the computational complexity from $O(n^2)$ to $O(n \log n)$, making it practical for large datasets. The FFT is an efficient algorithm for computing the discrete Fourier transform (DFT) and its inverse. By converting the functions into histograms, we can apply the FFT to perform the convolution in the frequency domain and then use the inverse FFT to transform the result back into the rapidity domain. For instance, we will use it to compute the middle convolution in $(\mathrm{CB} \otimes G + G) \otimes (\mathrm{CB} \otimes G + G)$, the $\mathrm{CB} \otimes G$ will be taken care of by the Gauss-Kronrod method.

3.4.3 Monte Carlo Convolution of Two Functions

To verify the correctness of our analytical and numerical convolutions, we use Monte Carlo convolution [29]. This involves generating random samples from the two functions we wish to convolve and then combining these samples to produce a new distribution. By comparing the resulting histogram from the Monte Carlo convolution with those obtained from analytical and numerical methods, we can check for consistency.

Monte Carlo convolution works by:

1. Generating a random number based on the first distribution function.
2. Generating a random number based on the second distribution function.
3. Summing the two numbers (one from each function) and filling it into a histogram.
4. Repeating steps 1-3 until we are satisfied with the number of entries in the histogram.

This method is particularly useful when dealing with complex functions for which analytical or numerical methods are challenging or infeasible.

3.5 Acquisition of ECMs Spread from Detector Output

To determine the functions that best fit our histograms, we conducted several trials and ultimately chose a custom function consisting of a smeared CB function plus a Gaussian.This function has eight parameters: the core sigma of the CB σ_{CB}, a shared mean μ, the α and n parameters of the CB, the smearing sigma σ_2, the sigma of the Gaussian σ_3, and normalization factors for both components. Importantly, this function is normalized, so adjusting the parameters (excluding the normalization factors) does not affect its integral.

3.5.1 Fitting the Resolution Histograms

We fitted this custom function to both partial-resolution histograms. The *ee* rapidity histogram exhibits a purely Gaussian character. All fittings were performed on two datasets: one with a beam rapidity smear σ_{ee} of 4.707×10^{-4}, and one where the beam rapidity was modeled as a delta function (no smear, $\sigma_{\text{ee}} = 0$). Shown fits on (Figure 3.4) are those of $\sigma_{\text{ee}} = 4.707 \times 10^{-4}$ as the resolution functions of the data without smearing were the same and $f_{ee}(y_{\text{ee}})$ was a delta function. The graphs also contain pulls; "pulls" are statistical measures used to quantify the difference between observed data and theoretical predictions, normalized by the uncertainty, often used in high-energy physics.

3.5.2 Convolution Properties and Parameter Reduction

Using the properties of convolution, we expressed the convolution of the beam spread ($f_{ee}(y_{\text{ee}})$) and the Truth Resolution Function (R_{truth}) as follows:

$$(\text{CB} \otimes G_1 + G_2) \otimes G_3 = \text{CB} \otimes G_1 \otimes G_3 + G_2 \otimes G_3 = \text{CB} \otimes G_{13} + G_{23}, \quad (3.9)$$

where G_{12} is a Gaussian function with parameters $\sigma_{12}^2 = \sigma_1^2 + \sigma_2^2$ and $\mu_{12} = \mu_1 + \mu_2$, likewise for G_{13}. Given these properties, we computed the convolution of the beam spread ($f_{ee}(y_{\text{ee}})$) and R_{truth} by simply adjusting the parameters, as the beam spread has a Gaussian character. In this way, we create function $F' = R_{\text{truth}} \otimes_{par} f_{ee}(y_{\text{ee}})$,

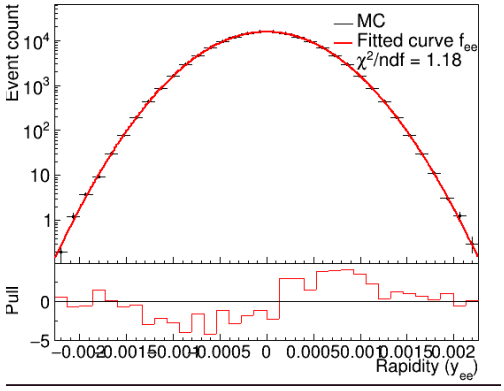

(a) Beam rapidity histogram fitted by $f_{ee}(y_{\text{ee}})$ with pulls.

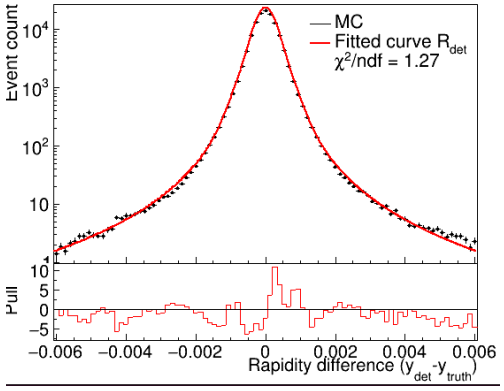

(b) Detector resolution histogram fitted by R_{det} with pulls.

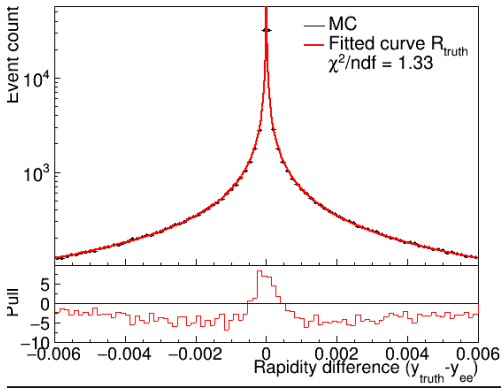

(c) Truth resolution histogram fitted by R_{truth} with pulls.

Figure 3.3 Function fitting with pulls. Both the resolution functions and the beam spread function fits are based on minimizing χ^2/ndf.

where $\otimes_{par}$ stands for convolution by altering the sigma parameters. To verify the correctness of this approach, we compared the result with the truth-level muon rapidity histogram (y_{truth}) and with the Monte Carlo convolution of the $f_{ee}(y_{\text{ee}}) \otimes_{mc} R_{\text{truth}}$ (Figure 3.4(a)).

Following this verification, we convolved the resulting function F' numerically, using the FFT method, with the Detector Resolution Function (R_{det}), and checked against the detector-level muon rapidity histogram (y_{det}) and the Monte Carlo convolution of all three functions ($R_{\text{det}} \otimes_{mc} R_{\text{truth}} \otimes_{mc} f_{ee}(y_{\text{ee}})$). Since the beam spread acts as a single parameter (σ_{ee}) in the overall convolution, we removed it to obtain the $R_{\text{det}} \otimes R_{\text{truth}}$ function. We then transformed this into a function F with a single parameter σ_{ee}^2, which we fitted to the detector-level muon rapidity histogram and received $\sigma_{\text{ee}} = 4.771(6) \times 10^{-4}$ which is not very far of from the actual value $\sigma_{\text{real}} = 4.708 \times 10^{-4}$. All of those 4 distribution are shown on (Figure 3.4(b)). The $F' \otimes_{fft} R_{\text{det}}$ (Green) and F (Red) are almost the same, as the sigma parameter didn't change much during the fitting.

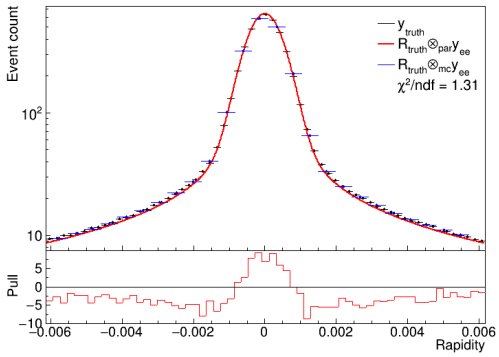

(a) Truth-level convolutions with pulls. Convolution made by altering the sigma parameters $F' = R_{\text{truth}} \otimes_{par} f_{ee}(y_{\text{ee}})$ (Red), Monte Carlo convolution of $f_{ee}(y_{\text{ee}}) \otimes_{mc} R_{\text{truth}}$ (Blue), Truth-level muon rapidity histogram (Black) and χ^2/ndf of Truth-level muon rapidity histogram vs F'.

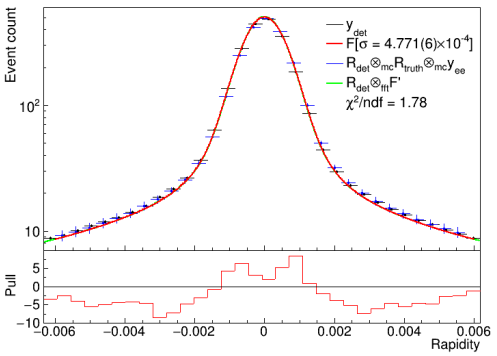

(b) Detector-level convolutions and F fit with pulls. FFT convolution $R_{\text{det}} \otimes_{fft} F'$ (Green), Monte Carlo convolution ($R_{\text{det}} \otimes_{mc} R_{\text{truth}} \otimes_{mc} f_{ee}(y_{\text{ee}})$ (Blue), Detector-level muon rapidity histogram (Black), One parameter function F fitted on detector-level muon rapidity histogram (Red) and χ^2/ndf of Detector-level muon rapidity histogram vs F.

Figure 3.4 Resolution functions convolved with f_{ee}, compared to truth-level and detector-level muon rapidity spread. Contains χ^2/ndf, convolutions made by the Monte Carlo method, and pulls.

3.5.3 Testing and Calibration Curve

Next, we applied this single-parameter function to another six simulated datasets to derive a calibration curve. Below is a table (Table 3.1) containing all relevant information, including the statistical uncertainties of measured parameters; the i stands for an imaginary unit, as the squared value corresponding to it was negative. Also, there are 2 versions of the calibration curve. In the first (Figure 3.5(a)), we use σ_{measured} parameter that we obtained from the fit and σ_{real}, which was known from the simulated data sets. If our method was perfect, we would expect the regressions in the form of $y = ax + b$ to have $a = 1$ and $b = 0$. That is not the case, but the fit is close. In the second calibration curve (Figure 3.5(b)), their squared values are used because the $\sigma^2_{\text{measured}}$ parameter that we are actually getting from the fit yielded a negative value for the data without smearing. Therefore, it cannot be included in the first one, and it's not part of the regression in the second one. We can see that even the result from data without any smear is fairly close to the curve. This point doesn't hold any real value for our curve, as it wasn't used in the regression. However, it shows that our method isn't too far off, even for values far from the relevant ones.

The third and final calibration curve (Figure 3.6) also incorporates the direct relationship between rapidity spread and ECMs spread. The relationship between rapidity spread and center-of-mass energy spread in positron-electron collisions can be expressed through the following derivation: E_{CMS} in positron-electron collisions is defined as:

$$E_{\text{CMS}} = 2\sqrt{E_{e^+}E_{e^-}} \tag{3.10}$$

Data	σ_{real} $[10^{-4}]$	σ^2_{real} $[10^{-7}]$	σ_{measured} $[10^{-4}]$	$\sigma^2_{\text{measured}}$ $[10^{-7}]$
Original	4.708	2.216	4.771(6)	2.276(6)
No Smearing	0	0	i1.331(8)	-0.177(2)
$E_{\text{CMS}} = 4.0$ MeV	3.781	1.429	3.799(6)	1.443(5)
$E_{\text{CMS}} = 4.5$ MeV	4.254	1.809	4.308(6)	1.856(6)
$E_{\text{CMS}} = 5.0$ MeV	4.726	2.233	4.804(6)	2.308(6)
$E_{\text{CMS}} = 5.5$ MeV	5.199	2.700	5.301(7)	2.811(7)
$E_{\text{CMS}} = 6.0$ MeV	5.672	3.209	5.800(7)	3.384(8)
$E_{\text{CMS}} = 6.5$ MeV	6.144	3.775	6.300(7)	3.970(9)

Table 3.1 Table of real σ_{real} and measured σ_{measured} rapidity spread values for different data sets.

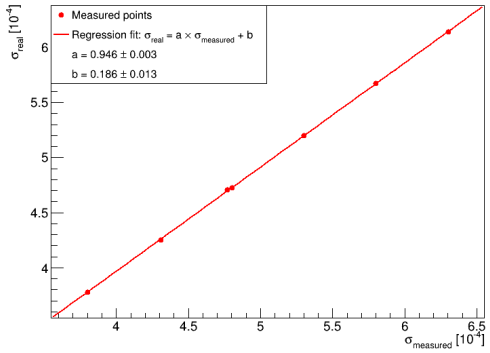

(a) Calibration Curve for $\sigma_{\text{real}}(\sigma_{\text{measured}})$ with linear regression.

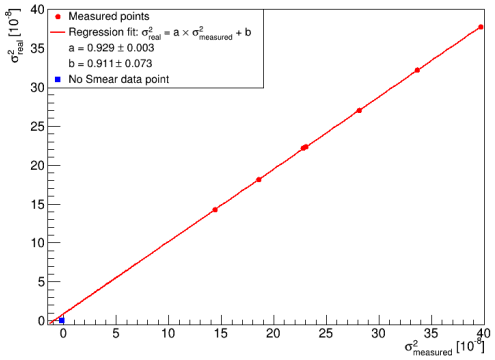

(b) Calibration Curve for $\sigma^2_{\text{real}}(\sigma^2_{\text{measured}})$ with linear regression and with a data point from data without smearing shown but not included in the regression.

Figure 3.5 Calibration curves for σ_{measured}

Taking the logarithm of both sides yields:

$$2 \ln \frac{E_{\text{CMS}}}{2} = \ln E_{e^+} + \ln E_{e^-} \tag{3.11}$$

The boost β, defined as $\beta = \frac{E_{e^+} - E_{e^-}}{E_{e^+} + E_{e^-}}$, can be expressed as:

$$\ln \frac{1+\beta}{1-\beta} = \ln E_{e^+} - \ln E_{e^-} \tag{3.12}$$

The left-hand side is related to the rapidity y, i.e.:

$$2y = \ln E_{e^+} - \ln E_{e^-} \tag{3.13}$$

$\ln E_{e^+}$ and $\ln E_{e^-}$ are not sharp values, so the spread of the right sides of both 3.11 and 3.13 is the same. Therefore we can write:

$$\sigma \left(2 \ln \frac{E_{\text{CMS}}}{2} \right) = \sigma \left(2y \right) \tag{3.14}$$

$$\sigma \left(\ln E_{\text{CMS}} - \ln 2 \right) = \sigma \left(y \right) \tag{3.15}$$

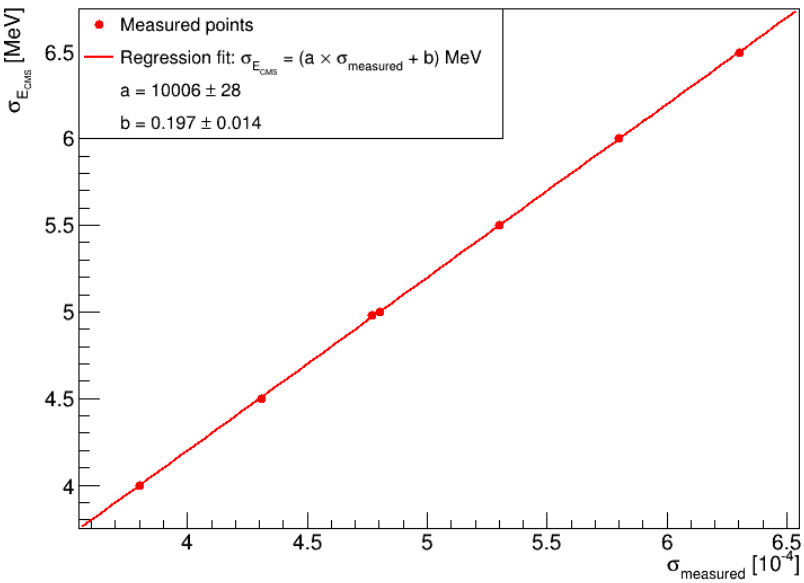

Figure 3.6 Calibration Curve for $\sigma_{\text{real}}(\sigma_{\text{measured}})$.

$$\sigma\left(\ln E_{\text{CMS}}\right) = \sigma\left(y\right) \tag{3.16}$$

Given that $\sigma\left(E_{\text{CMS}}\right) \ll E_{\text{CMS}}$, we can take the derivative of the left side and get:

$$\frac{1}{E_{\text{CMS}}}\sigma\left(E_{\text{CMS}}\right) = \sigma\left(y\right), \tag{3.17}$$

where at Belle II the beam energy is close to the $\Upsilon(4S)$ mass, i.e. $\simeq$10.58 GeV in the studied data. The calibration curve (Figure 3.6) provides a straightforward method for acquiring ECMs spread by fitting a single function to the detector output and applying a simple equation. Our final regression equation is:

$$\sigma_{E_{\text{CMS}}} = \left[(10006 \pm 28) \times \sigma_y + (0.197 \pm 0.014)\right] \text{ MeV} \tag{3.18}$$

Now, we would expect the regression parameter a to be equal to the $E_{\text{CMS}} \simeq$ 10580 MeV as derived in 3.17. Which makes our a 5% from the expected value.

3.6 Application on real data

Use our model F on the real data from the Belle II experiment, we first had to correctly convert them into rapidity histograms in CMS. The data consisting of 1223084 events were taken from about 400 separate runs, the same runs used in [24] , where each run ran on slightly different collision angles (Figure 3.7), so the Lorentz transformation to CMS had to be adjusted. Then, we fit our function F on the histogram (Figure 3.8), we just had to manually adjust the mean of F to the mean of real data rapidities, as it was shifted a bit and then it converged without any problems to the same value of $\sigma = 5.08(1) \times 10^{-4}$ for multiple choices of the values of initial sigma parameter. Then, by using the regression equation 3.18, we got a result for $\sigma_{E_{\text{CMS}}} = 5.28(1)$ MeV, where the uncertainty is just the statistic one.

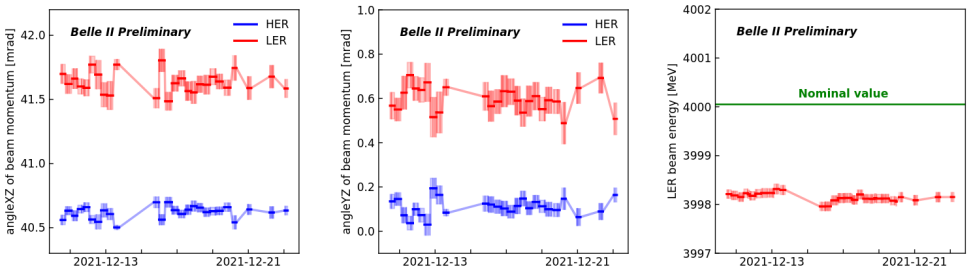

Figure 3.7 The time dependence of the electron (HER) and positron (LER) beam angles in the xz and yz plane. In addition, the positron beam energy is plotted on the right plot.[24]

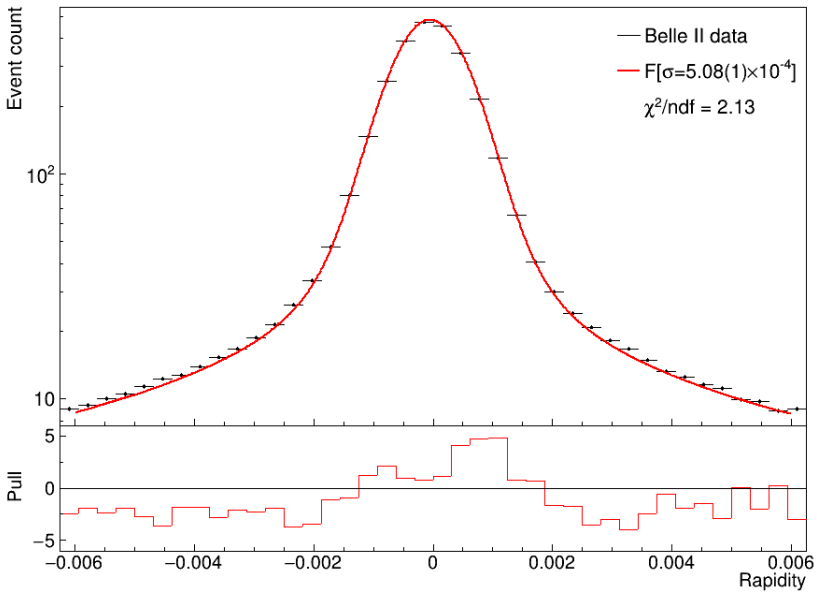

Figure 3.8 Real Belle II data fitted with F.

4 Discussion

The primary objective of this thesis was to develop a novel method to measure the center-of-mass energy spread ($\sigma_{E_{\text{CMS}}}$) using the rapidity of muons from $e^+e^- \to \mu^+\mu^-$ interactions recorded by the Belle II experiment. This approach leverages the high precision and statistical power of muon rapidity measurements, offering an independent and potentially more accurate method compared to a traditional technique based on B meson CMS energy, which is reliant on the shape of $\Upsilon(4S)$ resonance.

Our result of $\sigma_{E_{\text{CMS}}} = 5.28(1)$ MeV can be compared to 2 other results. The first result is from the method based on B meson energy used in [5], which measured $\sigma_{E_{\text{CMS}}}^{\text{B meson}} = 5.4(5)$ MeV. Our results match, and we believe that our method will have smaller systematic uncertainties than the B meson one; the improvement in the statistical uncertainty is evident. The second result comes directly from the SuperKEKB accelerator experts and is based on parameters of the accelerator optics [23] with the electron beam spread of 4.41 MeV and the positron beam spread of 3.08 MeV, which makes $\sigma_{E_{\text{CMS}}}^{\text{SuperKEKB}} = 5.26$ MeV. The $\sigma_{E_{\text{CMS}}}^{\text{SuperKEKB}}$ should have lower uncertainty than $\sigma_{E_{\text{CMS}}}^{\text{B meson}}$, however the exact uncertainty in unknown.

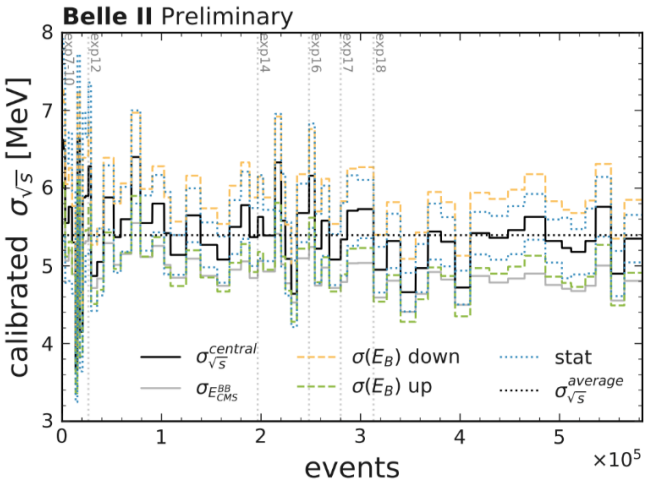

Figure 4.1 The corrected $\sigma_{\sqrt{s}}$ values (i.e., $\sigma_{E_{\text{CMS}}}$) and the various uncertainties are shown for the events used in the tau mass analysis. The average value of $\sigma_{\sqrt{s}}$ during this data-taking period is estimated as $\sigma_{\sqrt{s}}^{\text{average}} = 5.4(5)$ MeV [5]. The x axis is related to the time-axis as it spans over three years of the data taking (2019-2021). It can be seen that within the large uncertainties, the spread is consisted with a constant.

We can make an estimation of our result's systematic uncertainty by taking the real rapidity spread value from data $\sigma_y^{\text{real}} = 5.08(1) \times 10^{-4}$ and the model value by putting it into the calibration curve's regression (Equation in Figure 3.5(a)) to get $\sigma_y^{\text{model}} = 4.99 \times 10^{-4}$ which makes a 2% uncertainty (taking fit bias as the model uncertainty). The other sources of uncertainty, like the precision of the detector simulation or the precision of the parameters entering the Lorentz transformation, are not considered in this thesis. However, we believe they will be significantly lower than those of the B meson method of $\simeq 10\%$. The high statistical precision of the result would allow us to see changes in the energy spread in time and monitor the accelerator performance.

Our method's precision could be improved by employing more complex functions for smoother fitting and, thus, more precise convolutions. The truth-level resolution function, which was fundamental in the final convolution, could use a better fit on its steep peak. Truth-level resolution functions accurate determination is paramount, as it uses the sigma parameter of the rapidity beam spread directly.

The robustness of the method was tested using MC samples with a wide range of CMS energy spreads. By fitting the convolution-derived function to the rapidity distributions obtained from real data, we were able to extract $\sigma_{E_{\mathrm{CMS}}}$ with a high degree of statistical confidence.
An accurate knowledge of E_{CMS} spread will also improve the E_{CMS} precision, which is crucial in knowing if the accelerator runs in the right operation point - the $\Upsilon(4S)$ resonance, where the B mesons thrive. The E_{CMS} measurement based on B meson method will be improved if its E_{CMS} spread input is known better, as it can't measure it very well on its own (see Figure 4.1).

The next step for the development of our method would be systematic uncertainty derivation, including the detector simulation uncertainties, Lorentz transformation parameters uncertainties used in the transformation to CMS, and revision of the fitting functions - our model's uncertainty, as mentioned above.

Conclusion

In conclusion, this thesis presents a new method for measuring the center-of-mass energy spread in e^+e^- collisions using the rapidity of muons from $e^+e^- \to \mu^+\mu^-$ interactions. The method's robustness is validated through extensive simulations and application to real data, yielding precise and reliable $\sigma_{E_{CMS}}$ values.

The successful implementation and validation of this technique will enhance the Belle II experiment's capability to perform high-precision measurements. By improving the accuracy of E_{CMS} spread measurements, this method supports more precise determinations of particle masses and other fundamental parameters, ultimately advancing our understanding of particle physics and the Standard Model.

Future work should focus on further refining this method, especially by deriving the systematic uncertainties, exploring its application to other collision energy regimes, and integrating it with complementary measurement techniques for a comprehensive approach to high-precision energy calibration at Belle II and similar experiments.

Bibliography

1. Patrignani, C. et al. Review of Particle Physics. *Chin. Phys. C*. 2016, vol. 40, no. 10, p. 100001. Available from doi: 10.1088/1674-1137/40/10/100001.
2. Aad, Georges et al. Observation of a new particle in the search for the Standard Model Higgs boson with the ATLAS detector at the LHC. *Phys. Lett. B*. 2012, vol. 716, pp. 1–29. Available from doi: 10.1016/j.physletb.2012.08.020.
3. contributors, Wikipedia. *Standard Model - Wikipedia, The Free Encyclopedia*. 2024. Available also from: https://en.wikipedia.org/wiki/Standard_Model. [Online; accessed 19-June-2024].
4. Altmannshofer, W. et al. The Belle II Physics Book. *PTEP*. 2019, vol. 2019, no. 12, 123C01. Available from doi: 10.1093/ptep/ptz106. [Erratum: PTEP 2020, 029201 (2020)].
5. De La Cruz-Burelo, E. et al. *Beam energy corrections for the tau mass measurement*. [N.d.]. Internal text, not publicly available.
6. Committee, Nobel Prize. *The Nobel Prize in Physics 2008* [https://www.nobelprize.org/prizes/physics/2008/summary/]. 2008. Awarded to Yoichiro Nambu, Makoto Kobayashi, and Toshihide Maskawa.
7. Liptak, Z. J. et al. *Measurements of Beam Backgrounds in SuperKEKB Phase 2*. 2021.
8. Abe, T. et al. Belle II Technical Design Report. 2010. Available from arXiv: 1011.0352 (physics.ins-det).
9. Zlebčík, R. *Precision Measurement of Tau Lepton Mass at Belle II* [https://indico.cern.ch/event/1253107/contributions/5332457/attachments/2629497/4547735/Skala_Zlebcik.pdf]. 2024. Presentation at CERN Indico event, Mala Skala.
10. Adachi, I. et al. Measurement of the tau-lepton mass with the Belle II experiment. *Phys. Rev. D*. 2023, vol. 108, no. 3, p. 032006. Available from doi: 10.1103/PhysRevD.108.032006.
11. *Tau lepton mass is measured at Belle II with the highest precision to date.* [https://www.desy.de/news/news_search/in-dex_eng.html?openDirectAnchor=2781&two_columns=1.]. [N.d.]. Accessed: 2024-05-31.
12. Achasov, MN; Mo, XH; Muchnoi, NY, et al. Tau mass measurement at BES-III. *EPJ Web of Conferences*. 2019, vol. 08005. Available also from: https://inspirehep.net/files/b508410ca94d471d900c185ca11ba206.
13. Navas, S. et al. Review of Particle Physics - $B^{\pm}$. *Phys. Rev. D*. 2024, vol. 110, no. 3, p. 030001. Available also from: https://pdg.lbl.%20gov/2024/listings/rpp2024-list-B-plus-minus.pdf.
14. Navas, S. et al. Review of Particle Physics - B^{0}. *Phys. Rev. D*. 2024, vol. 110, no. 3, p. 030001. Available also from: https://pdg.lbl.%20gov/2024/listings/rpp2024-list-B-zero.pdf.

15. Aaij, R. et al. Observation of a J/$\psi\Lambda$ Resonance Consistent with a Strange Pentaquark Candidate in B-$\to$J/$\psi\Lambda$p$^-$ Decays. *Phys. Rev. Lett.* 2023, vol. 131, no. 3, p. 031901. Available from DOI: 10.1103/PhysRevLett.131.031901.

16. *Mandelstam variables* [https://en.wikipedia.org/wiki/Mandelstam_variables]. [N.d.]. Accessed: 2024-07-11.

17. *ROOT software library* [https://root.cern]. [N.d.]. Accessed: 2024-07-05.

18. James, F. *CERN Program Library Long Writeup D506: Function Minimization and Error Analysis*. Geneva, Switzerland, [n.d.]. Version 94.1. Available also from: https://cds.cern.ch/record/2296388/files/minuit.pdf.

19. *ROOT PlottingHelper* [https://github.com/zleba/PlottingHelper]. [N.d.]. Accessed: 2024-07-08.

20. *Monte Carlo Method* [https://en.wikipedia.org/wiki/Monte_Carlo_method]. [N.d.]. Accessed: 2024-07-05.

21. Rong-Gang, Ping. Event generators at BESIII. *Chinese Physics C*. 2008, vol. 32, no. 8, pp. 599–602. Available from DOI: 10.1088/1674-1137/32/8/001.

22. Allison, J. et al. Recent developments in Geant4. *Nuclear Instruments and Methods in Physics Research Section A: Accelerators, Spectrometers, Detectors and Associated Equipment*. 2016, vol. 835, pp. 186–225. ISSN 0168-9002. Available from DOI: https://doi.org/10.1016/j.nima.2016.06.125.

23. Adachi, I. et al. Measurement of the integrated luminosity of data samples collected during 2019-2022 by the Belle II experiment. 2024. Available from arXiv: 2407.00965 [hep-ex]. Submitted for publication.

24. Zlebcik, R. CTD2022: The Tracking at Belle II. In: *Connecting the Dots Workshop 2022 (CTD2022)*. 2023. Available also from: https://doi.org/10.5281/zenodo.8119739.

25. *Wolfram Alpha Computational intelligence* [https://www.wolframalpha.com/]. [N.d.]. Accessed: 2024-07-09.

26. *Gauss-Kronrod quadrature formula* [https://en.wikipedia.org/wiki/Gauss-Kronrod_quadrature_formula]. [N.d.]. Accessed: 2024-07-09.

27. *Crystal Ball function* [https://en.wikipedia.org/wiki/Crystal_Ball_function]. [N.d.]. Accessed: 2024-07-09.

28. *Fourier transform* [https://en.wikipedia.org/wiki/Fourier_transform] [N.d.]. Accessed: 2024-07-09.

29. *Convolution of probability distributions* [https://en.wikipedia.org/wiki/Convolution_of_probability_distributions]. [N.d.]. Accessed: 2024-07-09.

List of Figures

List of Tables